Universal REFoCUS Beamforming With Spatial Weighting

ANDERS EMIL VRÅLSTAD [1] **(Graduate Student Member, IEEE),**
MAGNUS DALEN KVALEVÅG [1] **(Member, IEEE),**
OLE MARIUS HOEL RINDAL [2] **(Member, IEEE),**
AND SVEIN-ERIK MÅSØY [1]

[1]Department of Circulation and Medical Imaging, Norwegian University of Science and Technology (NTNU), 7491 Trondheim, Norway
[2]Department of Informatics, University of Oslo, 0316 Oslo, Norway
CORRESPONDING AUTHOR: A. E. VRÅLSTAD (anders.e.vralstad@ntnu.no)

ABSTRACT REFoCUS (Retrospective Encoding For Conventional Ultrasound Sequences) offers great flexibility by enabling synthetic aperture beamforming from conventional ultrasound sequences. This flexibility is beneficial for many aspects in medical ultrasound beamforming, including *e.g.* combination of different transmit waves, distributed sound speed estimation and common-midpoint gathers. REFoCUS beamforming also has image quality comparable to state-of-art methods such as Retrospective Transmit Beamforming (RTB). However, the previously published implementations of REFoCUS do not address clutter from sidelobes and grating lobes present in the data before the recovery. This reduces image quality due to potentially strong sidelobes and grating lobes, particularly when using REFoCUS in combination with micro-beamforming and matrix array probes. Recordings from micro-beamforming probes may thus not be compliant with the existing REFoCUS methods. We propose to solve the sidelobes and grating lobe issues by introducing a reformulation of REFoCUS that performs multistatic data recovery and beamforming in the time domain, allowing spatial weighting to remove clutter and noise. Spatial weighting is based on common beamforming principles and incorporates element directivity, dynamic F-number, beam geometry weighting, and grating lobe suppression. We also discuss how aperture sampling affects beamforming with REFoCUS. Spatially Weighted REFoCUS (SWR) and critical sampling of the transmit aperture show suppression of receive grating lobes in an *in vivo* setting with two different micro-beamforming matrix-array probes, leading to an increase in gCNR contrast from 0.44 to 0.96 in a fetal image and from 0.39 to 0.89 in a cardiac image.

INDEX TERMS Retrospective beamforming, image quality, micro-beamforming, sub-aperture processing.

I. INTRODUCTION

THE introduction of the REFoCUS algorithm simplifies Synthetic Transmit Focusing (STF) processing for arbitrary transmit sequences by decomposing the transmitted waves into single element transmits using the Huygens-Fresnel principle [1]. STF improves resolution by coherently compounding multiple transmit events with appropriate Time-of-Flight (TOF) compensation, creating improved focusing. REFoCUS beamforming is the combination of a dataset recovery/conversion into a multistatic dataset, also called Synthetic Transmit Aperture (STA) dataset, followed by multistatic STA beamforming.

The transmit TOF of conventional ultrasound sequences, such as focused, diverging, and plane wave, can be viewed as virtual source sequences [2], [3]. Although this is quite accurate for sequences such as plane and diverging waves, the virtual source model for focused transmissions has been shown to produce image discontinuity artifacts around the focal point [4], [5]. This has been addressed in further extensions of the model [6], [7]. These models have a

limited region where they are valid and adequate weighting or masking is needed for optimal STF [8]. In other words, calculating the correct TOF for all locations is somewhat cumbersome and inaccurate using virtual sources for focused transmit sequences. REFoCUS offers an elegant solution, at the expense of increased computational complexity, by converting the original dataset into a multistatic dataset.

The multistatic data set has a straightforward processing of STF because the transmit time-of-flight is simply modeled as an omnidirectional propagation path length from the element to an image pixel divided by the speed of sound. STA beamforming also enables more advanced beamforming techniques such as two-way aberration correction, combination of different transmit sequences, distributed sound speed estimation and common midpoint beamforming [9], [10], [11]. Acquisition of multistatic data sets, using STA, is not optimal for many medical ultrasound applications due to limited depth penetration, SNR, and harmonic generation compared to focused transmissions. However, the combination of focused transmissions and REFoCUS will produce sufficient second harmonic energy, increase SNR and penetration, and allow STA beamforming [1].

REFoCUS beamforming is, as all array beamformers, limited by physical properties and requirements for creating high-quality, artifact-free images. The angular sampling density on transmit is one such requirement and is studied for REFoCUS in [5]. The transmitted energy is limited by the directivity of the transducer elements and the geometry of the transmission beam. The physical design of the array will also contribute to the quality of the beamformed image, where the aperture size contributes to image resolution, sidelobe level, and the array element pitch determines the degree of the grating lobes. sidelobes and grating lobes are not desirable in conventional ultrasound image reconstructions and should not be recovered by REFoCUS. In this work, we will demonstrate the impact of sidelobes and receive grating lobes on REFoCUS in acquisitions using micro-beamforming and 2D matrix array probes.

Micro-beamforming uses application-specific integrated circuits in the probe to beamform groups of neighboring elements (or subapertures abbreviated SAPs) as a data compression procedure before transfer to the scanner [12]. Some 2D matrix array probes have thousands of elements and can electronically steer and focus in both the azimuth and elevation directions. Data compression is needed for such acquisitions to limit the cable size between the probe and scanner. The micro-beamforming in the SAPs is designed for conventional Retrospective Transmit Beamforming (RTB) with Multi-Line Acquisitions (MLA) trajectories. The micro-beamforming steers the elements to avoid grating lobes along the transmit trajectory and moves them off-axis. Thus, conventional 1MLA beamforming with Dynamic Receive Focusing (DRF) will not include the grating lobes. However, REFoCUS includes all trajectories in the recovery process and will therefore also include the SAP grating lobes, which is undesirable.

We distinguish between transmit and receive, sidelobes and grating lobes. Transmit lobes are not easily removed in receive beamforming because they cause off-axis energy to overlap with on-axis energy. Receive lobes cause on-axis energy to be visualized off-axis and can therefore be removed with spatial masking. SAP grating lobes are an example of receive lobes.

The published literature on REFoCUS does not address the presence of sidelobes and grating lobes directly when recovering the multistatic dataset. Some literature reframe multistatic recovery as an inverse problem with a Tikhonov-regularized pseudo-inverse to recover focused walking aperture transmit sequences more accurately [11], [13], [14], [15]. The regularized method is claimed to decode the focused walking aperture sequence more accurately than the conventional Adjoint method, but in some cases it will increase the noise [13], [14]. The purpose of this regularization is to produce artifact-free images and to improve image quality. We will investigate whether receive sidelobes and grating lobes can be avoided using regularized recovery and compare it with our proposed method using the Adjoint recovery and spatial weighting.

This paper proposes an extension of REFoCUS beamforming using spatial weighting and critical sampling of the transmit aperture during recovery and beamforming to increase image quality and produce artifact-free images. The theory behind the weighting and considerations for performing REFoCUS on matrix arrays is described in Section II. Our suggested REFoCUS algorithm is implemented in the time domain, and multistatic data set recovery and STA beamforming are combined into a single process. Thus, we show that regularization in the frequency domain is not required. The method described in Section III, is applied in two *in vivo* settings with visible receive sidelobes and visible receive grating lobes. The proposed method is compared with a Delay-And-Sum (DAS) beamformer using virtual source RTB and two published REFoCUS methods; the Adjoint and Tikhonov regularized methods [14]. The latter methods use spatial weighting only during beamforming and not during recovery/conversion. We focus this work on 2D BMode imaging using matrix array probes and the resulting images, provided in Section IV, are compared using a contrast metric. The results are discussed in Section V and a conclusion is drawn in Section VI.

II. THEORY

The coordinate system and an example of the imaging setup positions are visualized in Fig. 1. The point positions are defined as 3D euclidean vectors with bold vector notation, *e.g.* $\mathbf{v} = \begin{bmatrix} v_x, v_y, v_z \end{bmatrix}^T$.

A. TIME-DOMAIN REFoCUS BEAMFORMING

A general pixel-based array beamformer using a weighted Delay-And-Sum (DAS) is given as

$$b(\mathbf{r}) = \sum_{m=1}^{M} \sum_{k=1}^{N} w(\mathbf{r}, m, n)\, s(m, n, t(\mathbf{r}, m, n)), \qquad (1)$$
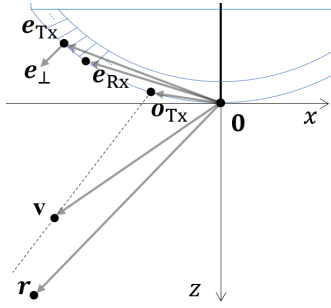
FIGURE 1. Visualization of the imaging setup with the coordinate system origin $0 = [0, 0, 0]^T$. The figure shows the transmit origin o_{Tx}, the receive element e_{Rx}, the transmit element e_{Tx}, the normal vector to an element $e_\perp$, the transmit focus position (virtual source) v, and the pixel position r.

where $w(\mathbf{r}, m, n)$ is a weighting function, $s(m, n, t)$ is the analytical channel data signal, and $t(\mathbf{r}, m, n)$ is the two-way Time-Of-Flight (TOF). The weighting function $w(\mathbf{r}, m, n)$ is spatially dependent incorporating multiple weighting functions such as element directivity, expanding aperture, beam geometry, and receive grating lobe suppression.

The beamformer performs both STF and Dynamic Receive Focusing (DRF) automatically by coherently compounding all N transmits and M receivers into the same coordinate grid. The two-way TOF is the sum of the transmit TOF $t_{Tx}(\mathbf{r}, n)$ and the receive TOF $t_{Rx}(\mathbf{r}, m)$. Time zero begins when the transmitted wave crosses the transmit origin $\mathbf{o}_{Tx}$. The receive TOF is given as

$$t_{Rx}(\mathbf{r}, m) = \frac{\|\mathbf{r} - \mathbf{e}_{Rx}(m)\|}{c}, \quad (2)$$

where $\mathbf{r}$ is the pixel position, $\mathbf{e}_{Rx}(m)$ is the m'th receive element and c is the speed of sound. The calculation of the transmit TOF $t_{Tx}(\mathbf{r}, n)$ depends on the transmit sequence and the chosen model [4], [5], [6], [7]. For multistatic beamforming, the transmit TOF is

$$t_{Tx}(\mathbf{r}, n) = \frac{\|\mathbf{r} - \mathbf{e}_{Tx}(n)\|}{c}, \quad (3)$$

with $\mathbf{e}_{Tx}(n)$ as the n'th transmit element.

The time domain recovery of the multistatic data set is implemented by introducing a new delay-and-sum over the original K transmit events. The procedure can be reformulated from the definition by Bottenus in [1] to

$$s(m, n, t) = \sum_{k=1}^{K} \hat{w}(k, n) s(m, k, (t + \tau(k, n))), \quad (4)$$

where $\hat{w}(k, n)$ is the applied aperture apodization, K is the number of original transmit events and $\tau(k, n)$ is the transmit delay used for the n'th transmit element ($\mathbf{e}_{Tx}(n)$) for the k'th transmit event. The transmit delay for a focused wave can be formulated as

$$\tau(k, n) = \frac{\|\mathbf{v}(k) - \mathbf{o}_{Tx}(k)\| - \|\mathbf{v}(k) - \mathbf{e}_{Tx}(n, k)\|}{c} \quad (5)$$

with virtual source position $\mathbf{v}$ and transmit origin $\mathbf{o}_{Tx}$, seen in Fig. 1. The original REFoCUS beamformer is two-fold; first recovering the multistatic data set using (4) and second, STA beamforming (1) using (2) and (3) for TOF. Note that the weighting function $\hat{w}$ for recovery in (4) does not depend on the position of the pixel $\mathbf{r}$. This means that all spatial points are relevant and included in multistatic recovery. As mentioned in Section I, the inclusion of signals from receive sidelobes and receive grating lobes in multistatic recovery can reduce image quality.

B. REFoCUS WITH MATRIX ARRAY PROBES
The use of transmit elements with elevation variation will have little effect on image quality for 2D BMode acquisitions. This is because a 2D BMode image acquisition only transmits in one elevation plane, and synthetic focusing is based on the angular diversity of multiple transmit directions. In the REFoCUS image reconstruction process, the number of transmit elements N can be reduced for 2D BMode imaging by reducing the 2D aperture to a 1D equivalent, with a negligible effect on image quality. Synthetic transmit focusing in azimuth and elevation simultaneously requires a 3D acquisition sequence, as recently shown by Bureau et al. [16].

C. HUYGENS-FRESNEL PRINCIPLE
The Huygens-Fresnel principle assumes Fraunhofer diffraction (spherical waves) of source elements to synthesize a wave field. In order to synthesize the transmitted wave field from a physical aperture, the source elements need adequate spacing according to the Fraunhofer region (far-field) given as

$$\|\mathbf{r} - \mathbf{e}\| > W_{pitch}^2/(2\lambda), \quad (6)$$

where $\|\mathbf{r} - \mathbf{e}\|$ is the distance from an element $\mathbf{e}$ and W_{pitch} is the spacing between elements [17]. The transmitted wave field synthesized with REFoCUS transmit elements is valid when the condition in (6) is met.

The REFoCUS decoding sum is a sum of spherical waves over the transmit aperture. This is similar to how some ultrasound simulators calculate the Rayleigh-Sommerfeld integral with the Huygens-Fresnel principle [18], [19]. Therefore, the REFoCUS sum of transmit elements is expected to apply an inherent beam weighting during beamforming. The strength of this weighting will increase with the number of summed transmit elements.

D. SPATIALLY WEIGHTED REFoCUS (SWR)
In order to enable spatial weighting of multistatic recovery, we bring recovery and beamforming together into one process. The universal beamformer using REFoCUS and Spatial Weighting (SWR) is given as

$$b(\mathbf{r}) = \sum_{m=1}^{M} \sum_{k=1}^{K} \sum_{n=1}^{N} w(\mathbf{r}, m, k, n) \, s(k, m, t(\mathbf{r}, m, k, n)), \quad (7)$$

where the two-way TOF $t(\mathbf{r}, m, k, n)$ includes the transmit delay reversal recovering the multistatic data set and the transmit and receive TOF from (3) and (2) respectively. The two-way TOF is expressed as

$$t(\mathbf{r}, m, k, n) = \frac{\|\mathbf{v}(k) - \mathbf{o}_{\text{Tx}}(k)\| - \|\mathbf{v}(k) - \mathbf{e}_{\text{Tx}}(n, k)\|}{c}$$
$$+ \frac{\|\mathbf{r} - \mathbf{e}_{\text{Tx}}(n, k)\|}{c} + \frac{\|\mathbf{r} - \mathbf{e}_{\text{Rx}}(m)\|}{c}, \quad (8)$$

where the first term is the transmit delay for the n'th transmit element used on the k'th transmit event (*e.g.* focused transmit beam). The second term in (8) is the propagation time from the transmit element to the pixel $\mathbf{r}$ and the third term is the receive TOF.

In order to obtain high image quality, we accommodate physical principles and use a spatially dependent weighting function $w(\mathbf{r}, m, k, n)$ during beamforming. Sections II-E to II-G describe the components of the weighting function.

E. ELEMENT DIRECTIVITY WEIGHTING

Both the transmitted and received amplitudes are governed by element directivity. Multistatic recovery with REFoCUS and beamforming, in general, should exclude out-of-sight directions to avoid increasing noise and include clutter [20]. The 1D directivity of an element is expressed as

$$D(\theta) = \text{sinc}\left(\frac{W}{\lambda}\sin(\theta)\right)\cos(\theta), \quad (9)$$

where θ is the azimuth angle from the element surface normal $\mathbf{e}_\perp$, W is the element width and λ is the wavelength [17]. The directivity function (9) is analogous to a constant F-number as a function of depth if a threshold value is evaluated [20]. For example, $D(\theta) = -3\text{dB} = 0.71$ will give a directivity angle $\theta_{-3\text{dB}} = 23°$ and the F-number 1.2 when the ratio $W/\lambda = 1$. The F-number is computed from the angle as

$$\text{F\#} = \frac{1}{2\tan(\theta)}. \quad (10)$$

The directivity and F-number weightings can be treated separately where the directivity weighting suppress clutter and the dynamic F-number weighting is often set to obtain a uniform resolution in the image (expanding aperture). A narrower element directivity (higher F-number) will trade off resolution. Here, we set the F-number using $D(\theta) = -3\text{dB} = 0.71$, resulting in a combined directivity and the F-number weighting given as

$$w_{\text{F\#}}(\mathbf{r}, m) = \begin{cases} 0.0 & \text{if } D(\theta(\mathbf{r}, m)) < 0.71 \\ D(\theta(\mathbf{r}, m)) & \text{otherwise,} \end{cases} \quad (11)$$

where

$$\theta(\mathbf{r}, m) = \angle(\mathbf{r} - \mathbf{e}(m), \mathbf{e}_\perp(m)), \quad (12)$$

and the element $\mathbf{e}(m)$ can be both a transmit element $\mathbf{e}_{\text{Tx}}$ or receiver element $\mathbf{e}_{\text{Rx}}$ indexed with n and m in (7) respectively. The operator $\angle(\cdot, \cdot)$ computes the angle between two vectors.
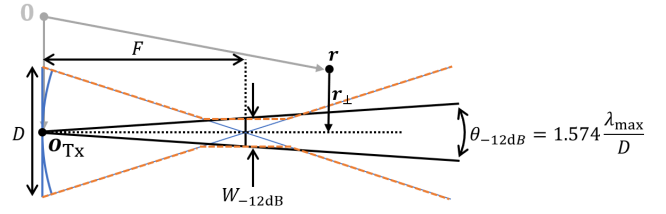

FIGURE 2. Beam geometry mask of a focused transmission beam.

The orientation of each element is given by its normal vector $\mathbf{e}_\perp$, illustrated in Fig. 1.

The element directivity weighting is used in all of the results presented in this paper.

F. BEAM GEOMETRY WEIGHTING

Another spatial limitation of array beamforming is the sidelobe level resulting from the diffraction of a finite array. Sidelobe signals are most often undesired and should ideally be suppressed. The signals received from outside the insonified region in transmit are unexpected in pulse echo imaging. Receive focusing of a strong scatter outside the insonified region may reconstruct significant sidelobes. This is undesirable, and weighting these sidelobes down is desired.

A model of the insonified region can be calculated from two lines that intersect the focal point and the edges of the transmitting array with an additional width around the focal point [6]. The beam width in the focus can be determined by the -12dB of the maximum opening angle of the focused beam $\theta_{-12\text{dB}} = 1.574\lambda_{\text{max}}/D$, expressed in (13) and visualized in Fig. 2 [17].

$$W_{-12dB} = F\tan(\theta_{-12\text{dB}}) = 2F\tan\left(1.574\frac{\lambda_{\text{max}}}{2D}\right), \quad (13)$$

where

$$\lambda_{\text{max}} = \frac{c}{f_{\text{min}}} \approx \frac{c}{f_{\text{burst}} - f_{\text{BW}}/2} \quad (14)$$

where c is the sound speed, D is the aperture size, $F = \|\mathbf{v} - \mathbf{o}_{\text{Tx}}\|$ is the focus depth, and f_{min} is the lowest included frequency in the received data. It is approximated by the center frequency of the transmitted pulse f_{burst} and the frequency bandwidth f_{BW}. The beam geometry weighting function is given as

$$w_{\text{BGW}}(\mathbf{r}, k) = \begin{cases} 1.0 & \text{if } \|\mathbf{r}_\perp\| < W_{-12\text{dB}}/2 \\ 1.0 & \text{if } \|\mathbf{r}_\perp\| \leq |D - \|\mathbf{r} + \mathbf{r}_\perp\| D/F|/2 \\ 0.0 & \text{otherwise,} \end{cases}$$
$$(15)$$

where $\|\mathbf{r}_\perp\|$ is the distance from pixel $\mathbf{r}$ to the transmitted scan line shown in Fig. 2.

The -12dB level is chosen because it includes a broader span than the more typical -6dB level. Broader inclusion is preferred in this case, because REFoCUS performs an intrinsic beam geometry weighting. This occurs because the

sum of spherical waves over the transmit aperture in (7), is a numerical calculation of the spatial impulse response using the Rayleigh-Sommerfeld integral and the Huygens-Fresnel principle [17]. Therefore, additional beam weighting may not be required, but it will benefit image quality in cases with high receive sidelobes. The attenuation strength of the weighting inherent in REFoCUS will increase with increasing number of transmit elements.

G. GRATING LOBE WEIGHTING

Array beamforming with a pitch larger than $\lambda/2$ for receiving elements will produce visible receive grating lobes when steering is applied. The original REFoCUS algorithm will, as a consequence, sum grating lobe signals when recovering and beamforming the multistatic dataset. An example where this is important is for SAP-based probes with micro-beamforming, as each SAP is typically larger than $\lambda/2$.

There are two sources of receive grating lobes when beamforming signals from SAP probes using REFoCUS. The first source of receive grating lobes is caused by the sum of the receiving elements into the SAP receivers, increasing the pitch. This first type of receive grating lobes is intrinsic to the collected signals and occurs away from the pre-steering direction of the SAP. It can be masked or weighted down during beamforming using the pixel-dependent weighting $w(\mathbf{r}, m, k, n)$ in (7).

The second source of receive grating lobes occurs in retrospective transmit if the REFoCUS transmit aperture with elements $\mathbf{e}_{\text{Tx}}$ is undersampled and has a pitch larger than the critical sampling pitch of $\lambda/2$. This occurs if we assume that $\mathbf{e}_{\text{Tx}}$ are the same as $\mathbf{e}_{\text{Rx}}$ in matrix arrays using SAP processing because the SAPs have a pitch larger than $\lambda/2$. This second type of receive grating lobes can be mitigated by weighting the grating lobes or by setting the number of REFoCUS transmit elements $\mathbf{e}_{\text{Tx}}$ to have a pitch $\lambda/2$.

The weighting of the grating lobes should include the angles within the sector θ_{include} around the steering angle θ_s, expressed as

$$\theta_{\text{include}} = \theta_s \pm \theta_g/2, \tag{16}$$

where angle θ_g is the periodicity of the grating lobes. For linear phased arrays, θ_g can be calculated as

$$\theta_g = \arcsin\left(\frac{c}{fW_{\text{pitch}}}\right), \tag{17}$$

where the highest frequency in the bandwidth $f = f_{\text{max}}$ should be used together with the sound speed c and the array pitch W_{pitch} [21]. Angles are visualized in Fig. 3. We assume the periodicity θ_g to be similar for curved arrays. The weighting function for the grating lobes is given as

$$w_G(\mathbf{r}, k) = \begin{cases} 1.0 & \text{if} \quad \theta_{\mathbf{vor}} < \theta_g \\ 0.0 & \text{otherwise}, \end{cases} \tag{18}$$

where $\theta_{\mathbf{vor}}(\mathbf{r}, k) = \angle(\mathbf{v}(k) - \mathbf{o}_{\text{Tx}}(k), \mathbf{r} - \mathbf{o}_{\text{Tx}}(k))$.
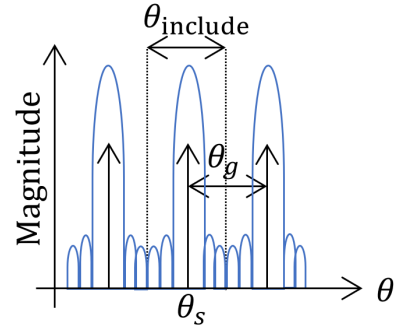

FIGURE 3. **Illustration of Grating Lobe Weighting.**

H. FULL WEIGHTING

By combining element directivity, beam geometry, and grating lobe weighting into the pixel-dependent weighting $w(\mathbf{r}, m, k, n)$ in (7), we can suppress noise and clutter before summation. This is not done by the original REFoCUS algorithm in (4) as $\hat{w}(k, n)$ is an aperture weight and does not depend on the pixel position $\mathbf{r}$. Suppression of clutter by pixel weighting during summation over transmit events k will not suffer from the resolution trade-off described in Section II-E. The full weighing is the product of the weightings described in (19). Note that the F-number weighing is applied for both the transmit and receive elements.

$$w(\mathbf{r}, m, k, n) = w_{\text{F\#}}(\mathbf{r}, m) \cdot w_{\text{F\#}}(\mathbf{r}, n) \cdot w_B(\mathbf{r}, k) \cdot w_G(\mathbf{r}, k), \tag{19}$$

where the subscripts B and G indicate the beam and grating lobe weighting respectively.

III. METHOD

A. PIXEL-BASED SOFTWARE BEAMFORMING

The software beamformer expressed in (7) is implemented with the python beamforming library *vbeam* [22]. The library is an open source pixel-based software beamformer built on top of the JAX library from Google [23] and is available on GitHub (github.com/magnusdk/vbeam).

The weights $w(\mathbf{r}, m, k, n)$ in (7) are calculated using the element directivity response from (9) for azimuth and elevation angles, the grating lobe weighting from (16), the beam geometry weighting from (15) and the active transmit aperture apodization. The element directivity weighting is set to zero for values below -3dB. In order to avoid striping artifacts, a smoothing function is applied laterally across the beam geometry weighting. A minimum width in the near-field is also added for the grating lobe weighting to ensure a non-zero pixel value. The beamforming process in *vbeam* is speedup, and memory is reduced by filtering out zero-weighted pixels, prior to delay and sum. The computer used to process the data has a NVIDIA RTX A5000 GPU and a 16 dual-core Intel Xeon Silver 4215R CPU.

The transmit elements are set along the center row of the 2D aperture because the scan sequence only steers in azimuth.

The reduction from a 2D transmit array to 1D for REFoCUS has negligible effect on the focusing quality because there is no synthetic focusing in elevation. In other words, we forced the transmit elements $\mathbf{e}_{Tx}$ to have a zero elevation component ($y = 0$) and chosen positions within the active transmit aperture to mimic the transmitted wave using the Huygens-Fresnel principle.

The Adjoint and Tikhonov regularized REFoCUS are processed using the code provided on GitHub (https://github.com/nbottenus/REFoCUS, DOI: https://zenodo.org/record/3473561) [14]. The MATLAB (The Mathworks, Inc., Natick, MA, USA) version of the process has been adapted to fit the framework of the UltraSound ToolBox (USTB) [24].

The multistatic recovery is implemented as a preprocess in USTB and the STA beamforming is processed using USTB's generalized beamformer. High-pass or ramp filtering after REFoCUS is in some cases essential for good image quality, as REFoCUS may introduce a gain of components in the low k-space [14]. The images shown in this paper were not filtered, as this gave negligible improvements or reduced image quality. The frequency domain REFoCUS recovery process runs in 16 parallel threads, and the STA beamforming uses the c++ MEX implementation of the generalized beamformer in USTB.

REFoCUS images of a single focused transmit events, used by Bottenus in [25], illustrate the geometry of the transmit beam. We use this to visualize clutter before and after spatial weighting and for different spacing's between elements $\mathbf{e}_{Tx}$ in the retrospective transmit aperture. The images are constructed by beamforming all pixels in the full scan sector for one single focused transmit.

All images are scan-converted, log-compressed ($20\log_{10}$) and visualized in MATLAB with tools from USTB [24].

B. WEIGHTINGS

Two acquisitions with 2D matrix array probes using SAP micro-beamforming technology are conducted to show the need for spatial weighting for REFoCUS (SWR).

Seven different beamforming methods are compared. The methods use different weighting functions $w(\mathbf{r}, m, k, n)$, synthetic focusing strategies, and different numbers of transmit elements for REFoCUS. All methods use a similar element directivity weighting as described in Section II-E. The F-numbers used are given in Table 1 and Table 2. The images are described as follows:

- RTB: Retrospective Transmit Beamforming using virtual sources. TOF is calculated with the unified pixel-based beamformer by Nguyen and Prager [6]. Grating lobe weighting (G) and beam geometry weighting (B) are also applied.
- ADJ: Adjoint REFoCUS. The retrospective transmit aperture is sampled with the same pitch as the receive SAPs.
- ADJ-C: Adjoint REFoCUS with critically sampled ($\sim \lambda/2$ pitch) transmit elements, as used on physical transmit.

TABLE 1. Settings for fetal *in vivo* channel data acquisition with Expert 22.

Parameter	Value	Units
System	Expert 22	-
Transducer array	eM6c (Gen.3)	-
Array geometry	2D curvilinear matrix array	-
Frequency	2.0/4.0	MHz
Focus depth	120	mm
Transmit beam step size	0.77	degrees
Tx and Rx F-numbers	1.04	-
Tikhonov γ	0.1	-
Grating lobe $\theta_{include}$	10.1	degrees

- TIK-C: Tikhonov Regularized REFoCUS with critically sampled ($\sim \lambda/2$ pitch) transmit elements, as used on physical transmit. The regularization factor $\gamma = 0.1$ is chosen to show the effect of the Tikhonov regularization. Higher values suppress the sidelobes and grating lobes better and produce images similar to ADJ-C.
- SWR-G: Spatially Weighted REFoCUS with grating lobe weighting (G) described in Section II-G. The retrospective transmit aperture is sampled with the same pitch as the receive SAPs.
- SWR-GB: Spatially weighted REFoCUS with grating lobe weighting and beam geometry weighting. The beam geometry weighting (B) is described in Section II-F. The retrospective transmit aperture is sampled with the same pitch as the receive SAPs.
- SWR-GBC: Spatially weighted REFoCUS with grating lobe weighting, beam geometry weighting, and critically sampled ($\sim \lambda/2$ pitch) transmit elements as used on physical transmit.

C. FETAL IMAGING

An *in vivo* fetal acquisition was recorded with the Voluson Expert 22 scanner and using the eM6c curvilinear matrix-array probe from GE HealthCare (GE HealthCare Women's Health Ultrasound, Zipf, Austria). The data are captured using a focused walking aperture transmit sequence, and the array uses receive SAP micro-beamforming. The recording was acquired from GE HealthCare's offices in Zipf, Austria. The patients provided written informed consent under a data collection agreement approved by the Upper Austrian Ethics Committee. The Voluson Expert 22 system allows pre-beamformed channel data (on SAP level) to be stored. The selected image presented here was chosen because it illustrates the effect of REFoCUS generated receive grating lobes very well. Table 1 describes the acquisition using the eM6c probe.

D. CARDIAC IMAGING

An *in vivo* cardiac acquisition was recorded using the Vivid E95 scanner and the 4Vc-D 2D matrix array probe

(a) RTB: Synthetic transmit focusing using virtual sources and spatial weighting.

(b) ADJ: Adjoint REFoCUS with Rx SAPs as Tx elements ($\sim 4\lambda$ pitch).

(c) ADJ-C: Adjoint REFoCUS with $\sim \lambda/2$ pitch for Tx elements as used on physical Tx.

(d) TIK-C: Tikhonov REFoCUS with $\gamma = 0.1$ and $\sim \lambda/2$ pitch for Tx elements as used in physical Tx.

(e) SWR-G: Spatially weighted REFoCUS with grating lobe weighting and Rx SAPs as Tx elements ($\sim 4\lambda$ pitch).

(f) SWR-GB: Spatially weighted REFoCUS with grating lobe- and beam geometry weighting. Using Rx SAPs as Tx elements ($\sim 4\lambda$ pitch).

(g) SWR-GBC: Spatially weighted REFoCUS with grating lobe and beam geometry weighting. Using critically sampled Tx elements with $\sim \lambda/2$ pitch similar to what is used on physical Tx.
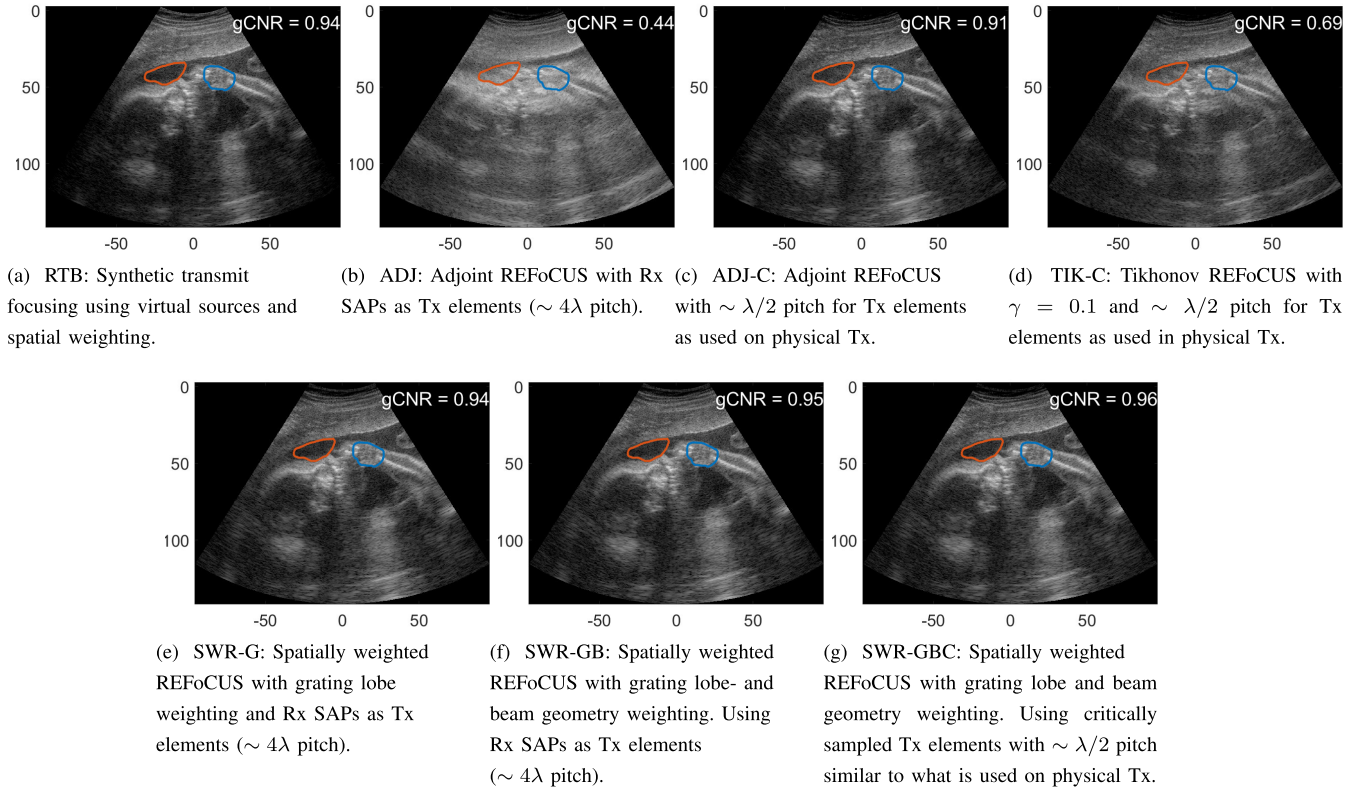
FIGURE 4. *In vivo* **fetal face image. The data are recorded with an eM6c probe using micro-beamforming. Comparison of different beamforming methods. The contrast is measured with gCNR and hand-drawn masks of tissue and cavity. Each image is plotted with 80dB dynamic range and normalized to its own max value. The axial and azimuthal axes are given in millimeters. A GIF containing the images is uploaded as supplementary material.**

TABLE 2. Settings for cardiac *in vivo* channel data acquisition with E95.

Parameter	Value	Units
System	E95	-
Transducer array	4Vc-D	-
Array geometry	2D matrix array	-
Frequency	1.7/2.8	MHz
Focus depth	90.8	mm
Transmit beam step size	0.802	degrees
Tx and Rx F-numbers	0.55	-
Tikhonov γ	0.1	-
Grating lobe θ_{include}	23.4	degrees

from GE HealthCare (GE Vingmed Ultrasound AS, Horten, Norway). The probe uses receive SAP micro-beamforming and focused phased transmits. The Vivid E95 also allows for storage of pre-beamformed channel data. The recording was acquired at St Olavs hospital, Trondheim, Norway. The patient provided informed consent in writing under a data collection agreement approved by the Mid-Norway Regional Committee for Medical and Health Research Ethics. A cardiac image with a strong scatterer in the heart wall was chosen to illustrate the effect of receive sidelobes and grating lobes. Table 2 describes cardiac acquisition parameters.

E. QUANTIFICATION of IMAGE QUALITY

In order to quantify clutter from grating lobes and noise, the contrast between low echoic regions and tissue regions are measured with the generalized Contrast-to-Noise-Ratio (gCNR) [26]. The gCNR measures the contrast as separability between the pixel intensity distributions of two regions of the image by measuring the overlap between them. Normalized histograms are used to estimate the distributions. Equation (20) expresses the calculation of gCNR.

$$\text{gCNR} = 1 - \sum_{n=1}^{N_{\text{bin}}} \min\left\{p_{\text{cavity}}(n), p_{\text{tissue}}(n)\right\}, \qquad (20)$$

where $p_{\text{cavity}}(n)$ is the distribution of pixel values inside the cavity, and $p_{\text{tissue}}(n)$ is the distribution of pixel values of the a tissue region. Histograms are calculated after log compression ($20 \log_{10} | \cdot |$) using $N_{\text{bin}} = 256$ bins.

IV. RESULTS
A. FETAL IMAGING

BMode images of the fetal SAP acquisition using different REFoCUS beamformers are visualized in Fig. 4. Images include hand-drawn regions of tissue and cavity, which are used to calculate the gCNR. The gCNR contrast values are plotted in the upper right corner of the figures. Images of
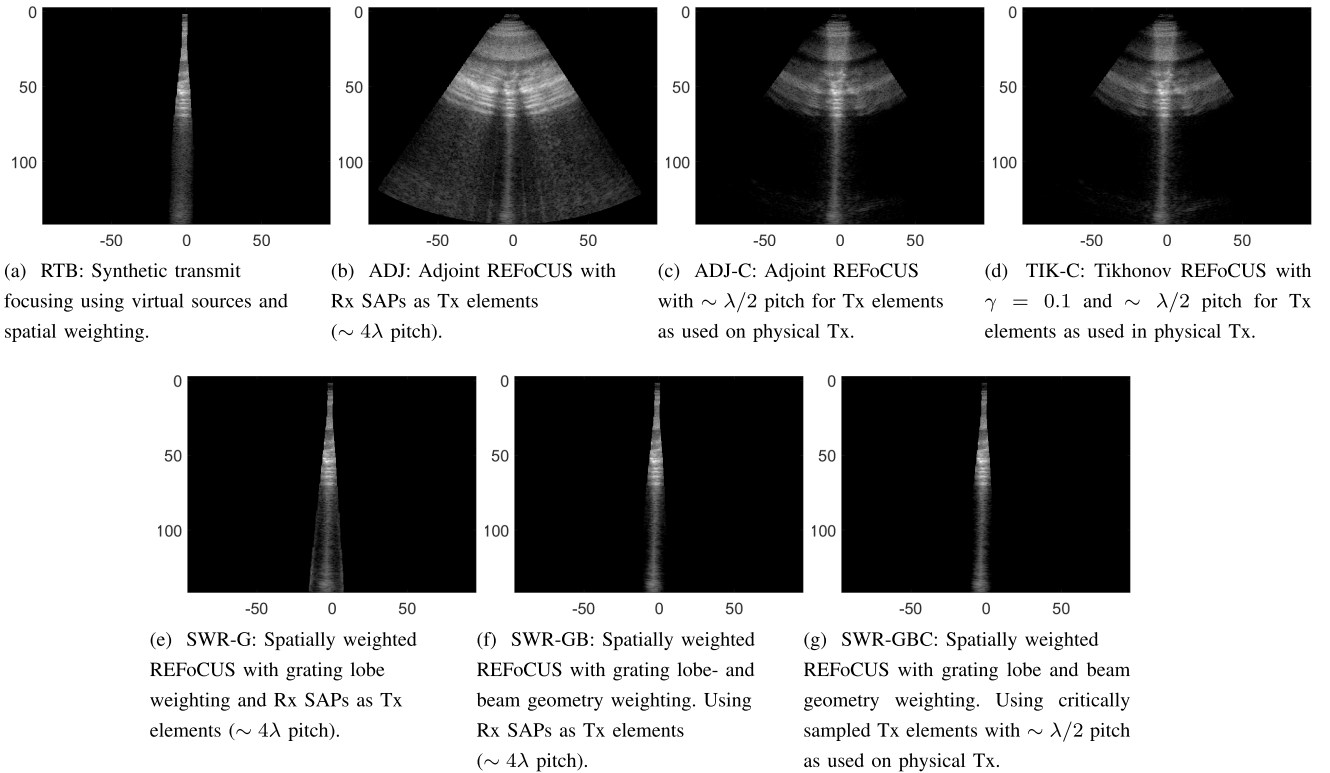
(a) RTB: Synthetic transmit focusing using virtual sources and spatial weighting.

(b) ADJ: Adjoint REFoCUS with Rx SAPs as Tx elements ($\sim 4\lambda$ pitch).

(c) ADJ-C: Adjoint REFoCUS with $\sim \lambda/2$ pitch for Tx elements as used on physical Tx.

(d) TIK-C: Tikhonov REFoCUS with $\gamma = 0.1$ and $\sim \lambda/2$ pitch for Tx elements as used in physical Tx.

(e) SWR-G: Spatially weighted REFoCUS with grating lobe weighting and Rx SAPs as Tx elements ($\sim 4\lambda$ pitch).

(f) SWR-GB: Spatially weighted REFoCUS with grating lobe- and beam geometry weighting. Using Rx SAPs as Tx elements ($\sim 4\lambda$ pitch).

(g) SWR-GBC: Spatially weighted REFoCUS with grating lobe and beam geometry weighting. Using critically sampled Tx elements with $\sim \lambda/2$ pitch as used on physical Tx.

FIGURE 5. Single focused transmit images of *in vivo* fetal face show in Fig. 4. The images are beamformed for the full sector scan. The data are recorded with an eM6c probe using micro-beamforming. Comparison of different beamforming methods demonstrates suppression of the grating lobe and sidelobe clutter outside of the beam geometry. Each image is plotted with 80dB dynamic range and normalized to its own max value. The axial and azimuthal axes are given in millimeters. A GIF containing the images is uploaded as supplementary material.

single focused transmit events using the same beamformer settings as in Fig. 4, are visualized in Fig. 5.

B. CARDIAC IMAGING

BMode images of the cardiac SAP acquisition are visualized in Fig. 6. The gCNR is indicated in the upper right corner of the figures. The additional beam geometry weighting in Fig. 6f suppresses the strong sidelobe visible in Fig.6e around z=140mm, x=−80mm. Fig. 8 shows the sidelobe levels of this point scatterer. The single focused transmit event images of the cardiac images are visualized in Fig. 7.

C. COMPUTATION

The recovery in ADJ, ADJ-C and TIK-C is implemented in the frequency domain and runs on the CPU, while RTB, SWR-G, SWR-GB and SWR-GBC are implemented in the time domain and runs on GPU. The frequency domain implementations are also divided into two processes; recovery and STA beamforming, while the time domain implementations recover and beamform in one step. To compare the computation between the methods more fairly, we additionally ran the time-domain ADJ-C method on the CPU. The computation time for the frequency domain, time domain, CPU, and GPU implementations is given in Table 3 for the fetal and cardiac images.

V. DISCUSSION

Grating lobe weighting is shown to suppress receive grating lobes, as expected. The receive grating lobes for fetal SAP acquisition are visible from the single transmit image in Fig. 5b and the weighting of the grating lobe is shown to successfully suppress them in Fig. 5e. The grating lobe weighting alone increases the gCNR measurement from 0.44 to 0.94, and further to 0.95 when also applying the beam geometry weighting, as shown in Fig. 4. The need for grating lobe weighting is also beneficial in the cardiac image. This is evident when comparing Fig. 6b and Fig. 6e where there is an increase from 0.53 to 0.87. The septum appears to repeat within the image in Fig. 6b. This repeatability (spatial aliasing) is clearer in the cardiac case than in the fetal case due to the high dynamic content in the cardiac image. Similarly, the cardiac image with beam geometry weighting shows sidelobe suppression more clearly than the fetal image because of the large dynamic contrast between a strong point scatter in the myocardium next to the region with low scattering inside the atrium.

Critical sampling of the transmit aperture in retrospective beamforming seems to remove some of the grating lobe clutter. The comparison of Fig. 5b and Fig. 5c shows this for the fetal image. This is expected because retrospective transmit grating lobes can be avoided by using a pitch $< \lambda/2$,
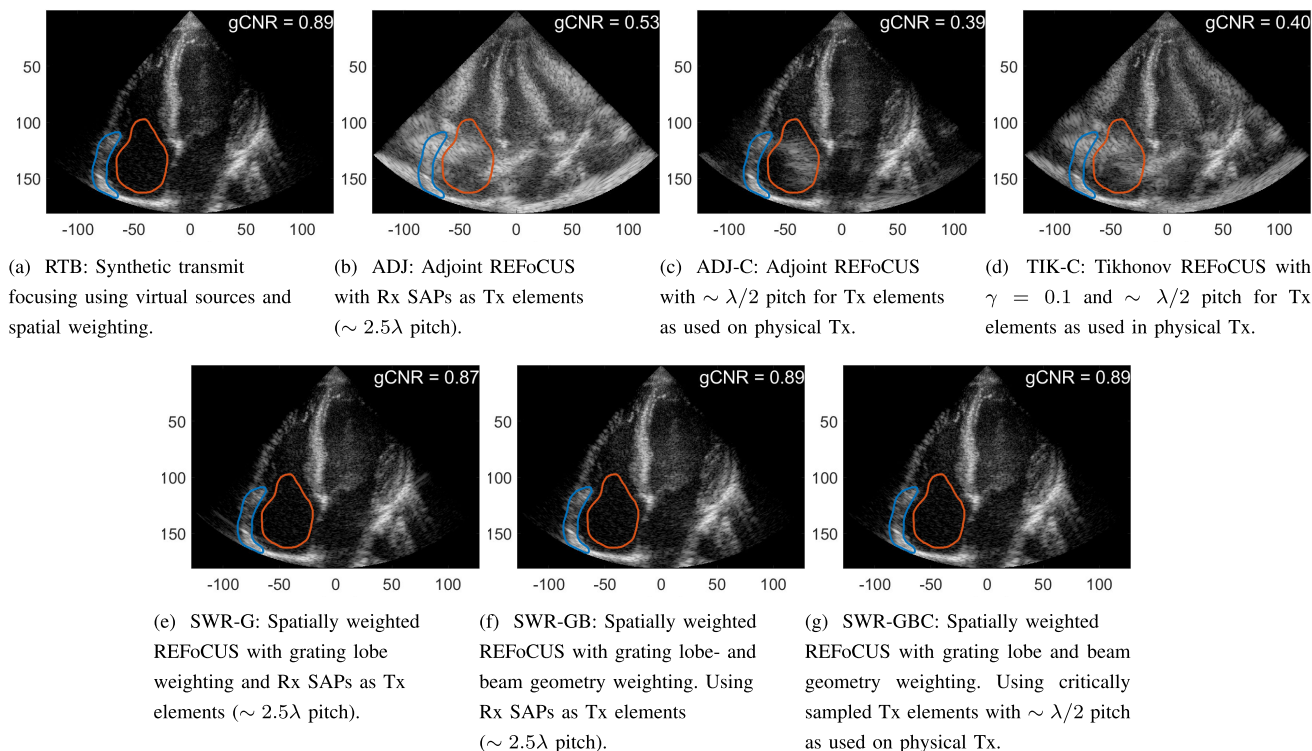
(a) RTB: Synthetic transmit focusing using virtual sources and spatial weighting.

(b) ADJ: Adjoint REFoCUS with Rx SAPs as Tx elements ($\sim 2.5\lambda$ pitch).

(c) ADJ-C: Adjoint REFoCUS with $\sim \lambda/2$ pitch for Tx elements as used on physical Tx.

(d) TIK-C: Tikhonov REFoCUS with $\gamma = 0.1$ and $\sim \lambda/2$ pitch for Tx elements as used in physical Tx.

(e) SWR-G: Spatially weighted REFoCUS with grating lobe weighting and Rx SAPs as Tx elements ($\sim 2.5\lambda$ pitch).

(f) SWR-GB: Spatially weighted REFoCUS with grating lobe- and beam geometry weighting. Using Rx SAPs as Tx elements ($\sim 2.5\lambda$ pitch).

(g) SWR-GBC: Spatially weighted REFoCUS with grating lobe and beam geometry weighting. Using critically sampled Tx elements with $\sim \lambda/2$ pitch as used on physical Tx.

FIGURE 6. *In vivo* cardiac four chamber image. The data were recorded with a 4Vc-D probe using micro-beamforming. Comparison of different beamforming methods demonstrates suppression of grating lobe and sidelobe clutter outside of the beam geometry. Each image is plotted with 60dB dynamic range and normalized to its own max value. The axial and azimuthal axes are given in millimeters. A GIF containing the images is uploaded as supplementary material.

TABLE 3. Computation time for different implementations of REFoCUS. Processed on a NVIDIA RTX A5000 GPU and on a 16 dual-core Intel Xeon Silver 4215R CPU.

Setting	Computation time for fetal image	Computation time for cardiac image
Frequency-domain recovery and time-domain STA beamforming of ADJ-C on CPU	2 min and 10 sec (1 min and 40 sec for recovery)	34 sec (21 sec for recovery)
Single stage time-domain ADJ-C on CPU	58 min and 33 sec	33 min and 50 sec
Single stage time-domain ADJ-C on GPU	19 sec (7 sec for XLA compilation)	13 sec (4 sec for XLA compilation)
Accelerated single stage time-domain SWR-GBC on GPU	14 sec (11 sec for XLA compilation)	12 sec (8 sec for XLA compilation)

as described in Section II-G. However, we cannot remove the grating lobes originating from the steered sum of the received signal in the SAP. Therefore, the grating lobe clutter from receive SAPs is expected and visible in Fig. 5c and Fig. 5d. The grating lobe weighting masks out the receive grating lobes as shown in Fig. 5e, increasing the gCNR in Fig. 4e.

Critical sampling of the retrospective transmit aperture also suppresses some of the receive grating lobes for cardiac images, but not all. This is seen by comparing Fig. 7b, 7c and 7e. The ADJ-C in Fig. v has lower grating lobes than the ADJ in Fig. 7b because retrospective transmit grating lobes are avoided. The SAP grating lobes intrinsic to the collected channel data are still present, but can be masked out as shown in Fig. 7e. A SAP grating lobe is visible in the right atrium in Fig. 4c. The grating lobe is removed using spatial weighting in Figs. 4e-4g, as also indicated by the increase in gCNR.

The beam geometry weighting is shown to be beneficial for contrast. Some noise along the edge of the grating lobe weighting is seen in Fig. 5e. The introduction of beam geometry weighting in Fig. 5f appears to suppress some of this clutter. The clutter also seems to be suppressed for the methods using critically sampled retrospective transmit apertures, ADJ-C and TIK-C. This is expected because the inherent beam weighting in REFoCUS will more strongly attenuate the sidelobes when using a higher number of REFoCUS transmit elements. The beam geometry weighting also shows a clear suppression of the strong receive sidelobe visible in Fig. 6e around z=140mm, x=−80mm. The sidelobes are also visible in Fig. 6c and Fig. 6d, but they
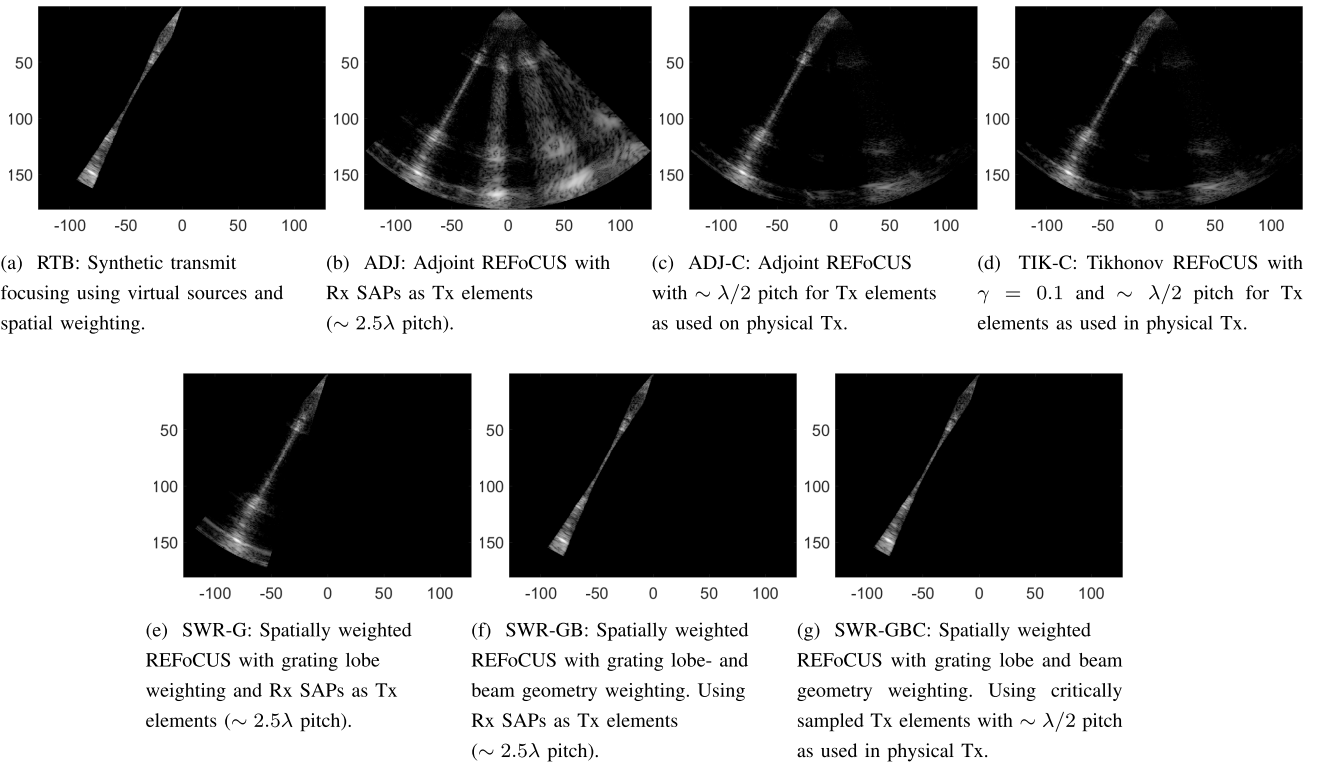
(a) RTB: Synthetic transmit focusing using virtual sources and spatial weighting.

(b) ADJ: Adjoint REFoCUS with Rx SAPs as Tx elements ($\sim 2.5\lambda$ pitch).

(c) ADJ-C: Adjoint REFoCUS with $\sim \lambda/2$ pitch for Tx elements as used on physical Tx.

(d) TIK-C: Tikhonov REFoCUS with $\gamma = 0.1$ and $\sim \lambda/2$ pitch for Tx elements as used in physical Tx.

(e) SWR-G: Spatially weighted REFoCUS with grating lobe weighting and Rx SAPs as Tx elements ($\sim 2.5\lambda$ pitch).

(f) SWR-GB: Spatially weighted REFoCUS with grating lobe- and beam geometry weighting. Using Rx SAPs as Tx elements ($\sim 2.5\lambda$ pitch).

(g) SWR-GBC: Spatially weighted REFoCUS with grating lobe and beam geometry weighting. Using critically sampled Tx elements with $\sim \lambda/2$ pitch as used in physical Tx.

FIGURE 7. Single focused transmit images of *in vivo* cardiac four chamber show in Fig. 6. The images were beamformed for the full sector scan. The data were recorded with a 4Vc-D probe using micro-beamforming. Each image is plotted with 60dB dynamic range and normalized to its own max value. The axial and azimuthal axes are given in millimeters. A GIF containing the images is uploaded as supplementary material.
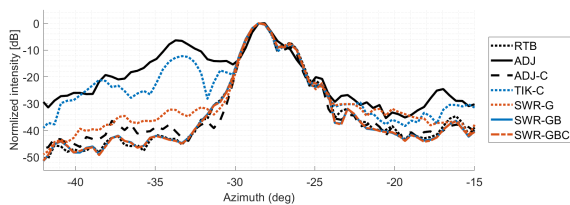

FIGURE 8. High echoic scatter in myocardium of Fig. 6. The line plots show the maximum pixel intensity along a depth interval $\pm \sim 2.5$mm from the scatterer. Each plot is normalized to its own maximum value.

have lower levels due to the inherent beam weighting in REFoCUS. Fig. 8 shows how the sidelobe levels of the strong scatterer are similar for RTB, SWR-GB and SWR-GBC, while being higher for the other methods. ADJ and TIK have the highest sidelobes due to the contribution of the receive grating lobes.

The critical sampling of the transmit aperture in Fig. 5g compared to the undersampling in Fig. 5f seems to benefit the image quality in the shallowest 4 cm, while having a negligible effect elsewhere. This is because the REFoCUS algorithm synthesizes the transmitted wavefield using the Huygens-Fresnel principle, and this is a valid approximation of the physical elements only in the Fraunhofer region, as described

in Section II-C. A pitch of 4λ will enter the Fraunhofer region at 8λ depth. This is around 4 cm depth for the lowest frequencies in the received bandwidth. The near field in the REFoCUS images becomes more similar to the near field in the RTB image when retrospectively using a pitch of $\lambda/2$. This is expected because RTB use virtual sources in transmit focus to compute TOF and do not suffer from near field diffraction as the REFoCUS transmit elements do.

The SWR-GBC is the REFoCUS method that seems to be most similar to RTB. This is because SWR-GBC uses the same spatial weighting as used for the RTB image, and because SWR-GBC avoids retrospective receive grating lobes in the near field. The gCNR for the fetal RTB image in Fig. 4a is 0.94, and 0.96 for the fetal SWR-GBC in Fig. 4a. This may be explained by the additional inherent beam weighting by REFoCUS. For the cardiac image, there is no difference in gCNR between RTB and SWR-GBC.

The Tikhonov regularization in Figs. 5d and 7d does not seem to suppress the sidelobes and grating lobes. The best image quality for TIK was obtained using a high regularization factor γ. A high γ creates images that are similar to the ones created by the Adjoint method. We therefore chose to illustrate the image with a lower value $\gamma = 0.1$.

It is evident from the computational measures in Table 3 that the frequency-domain recovery and time-domain STA

beamforming implementation is faster than our single-stage time-domain REFoCUS implementation when running on the CPU. However, as expected, our GPU implementation in the time domain seems to be faster. When also speeding up the GPU computation by only processing pixels with non-zero beam geometry weighting, the SWR-GBC uses only 14 and 12 seconds for the fetal and cardiac images, respectively. The XLA compilation, indicated in parentheses, is reduced from the total computation time when the processing is run a second time. This means that the second frame and beyond will only take 3 and 4 seconds to run the accelerated SWR-GBC on GPU. A potential method for further computational efficiency gain is to increase the pitch of the REFoCUS transmit elements dynamically with depth according to the Fraunhofer region; $\|\mathbf{r} - \mathbf{e}\| > \frac{W_{\text{pitch}}^2}{2\lambda}$.

Reduction of signal compounding by using spatial weighting will reduce the quality of focusing. The spatial weighting is employed to remove receive sidelobes and grating lobes. In scenarios without grating lobes and where the dynamic range of interest excludes the received sidelobes, spatial weighting is unnecessary. Beam geometry weighting may, for example, in such cases limit the coherent compounding and reduce the focusing quality. This is not only the case for REFoCUS, but also for other synthetic transmit focusing methods such as RTB with virtual sources.

The REFoCUS methods are powerful and enable advanced beamforming techniques for all conventional ultrasound scan sequences. The extension for 3D acquisitions is interesting for future work and can be implemented using the same formulation as presented in (7). Proper synthetic transmit focusing in elevation with REFoCUS requires a retrospective transmit aperture with $\lambda/2$ pitch in the elevation direction.

VI. CONCLUSION

The introduction of spatial weighting and critical aperture sampling during multistatic recovery and beamforming with REFoCUS has been shown to improve image contrast in scenarios where receive sidelobes and grating lobes are present. The results show artifact-free images with image quality similar to RTB. The proposed method enables the use of REFoCUS for micro-beamformed Sub Aperture technology commonly used for 2D matrix array probes. The generalization of REFoCUS presented here enables time-domain beamforming with REFoCUS and should, in principle, also improve image quality for all scan sequences and can be generalized to 3D imaging.

ACKNOWLEDGMENT

REFERENCES

[1] N. Bottenus, "Recovery of the complete data set from focused transmit beams," *IEEE Trans. Ultrason., Ferroelectr., Freq. Control*, vol. 65, no. 1, pp. 30–38, Jan. 2018.

[2] M.-H. Bae and M.-K. Jeong, "A study of synthetic-aperture imaging with virtual source elements in B-mode ultrasound imaging systems," *IEEE Trans. Ultrason., Ferroelectr., Freq. Control*, vol. 47, no. 6, pp. 1510–1519, Nov. 2000.

[3] C. H. Frazier and W. D. O'Brien, "Synthetic aperture techniques with a virtual source element," *IEEE Trans. Ultrason., Ferroelectr., Freq. Control*, vol. 45, no. 1, pp. 196–207, Jan. 1998.

[4] O. M. Hoel Rindal, A. R. Molares, and A. Austeng, "A simple, artifact–free, virtual source model," in *Proc. IEEE Int. Ultrason. Symp. (IUS)*, Oct. 2018, pp. 1–4.

[5] N. Bottenus, "Comparison of virtual source synthetic aperture beamforming with an element-based model," *J. Acoust. Soc. Amer.*, vol. 143, no. 5, pp. 2801–2812, May 2018. [Online]. Available: https://asa.scitation.org/doi/full/10.1121/1.5036733

[6] N. Q. Nguyen and R. W. Prager, "High-resolution ultrasound imaging with unified pixel-based beamforming," *IEEE Trans. Med. Imag.*, vol. 35, no. 1, pp. 98–108, Jan. 2016.

[7] N. Q. Nguyen and R. W. Prager, "Ultrasound pixel-based beamforming with phase alignments of focused beams," *IEEE Trans. Ultrason., Ferroelectr., Freq. Control*, vol. 64, no. 6, pp. 937–946, Jun. 2017.

[8] O. M. H. Rindal, A. Vrålstad, T. G. Bjåstad, A. Austeng, and S.-E. Måsøy, "Coherence from REFoCUS compared to retrospective transmit beamforming," in *Proc. IEEE Int. Ultrason. Symp. (IUS)*, Oct. 2022, pp. 1–4.

[9] D. Liu and K. Ustuner, "Aberration correction using broad transmit beams," in *Proc. IEEE Int. Ultrason. Symp.*, Oct. 2012, pp. 2270–2273.

[10] B. A. Herrera, N. J. Eshkalak, and N. Bottenus, "Improved spatiotemporal resolution in echocardiography using mixed geometry imaging sequences," *IEEE Trans. Ultrason., Ferroelectr., Freq. Control*, vol. 71, no. 4, pp. 438–447, Apr. 2024. [Online]. Available: https://ieeexplore.ieee.org/abstract/document/10426760

[11] R. Ali, T. Brevett, D. Hyun, L. L. Brickson, and J. J. Dahl, "Distributed aberration correction techniques based on tomographic sound speed estimates," *IEEE Trans. Ultrason., Ferroelectr., Freq. Control*, vol. 69, no. 5, pp. 1714–1726, May 2022.

[12] G. U. Haugen, K. Kristoffersen, and D. G. Wildes, "Ultrasound probe sub-aperture processing," U.S. Patent 2005 0113 699 A1, May 26, 2005.

[13] R. Ali, J. J. Dahl, and N. Bottenus, "Regularized inversion method for frequency-domain recovery of the full synthetic aperture dataset from focused transmissions," in *Proc. IEEE Int. Ultrason. Symp. (IUS)*, Oct. 2018, pp. 1–9.

[14] R. Ali, C. D. Herickhoff, D. Hyun, J. J. Dahl, and N. Bottenus, "Extending retrospective encoding for robust recovery of the multistatic data set," *IEEE Trans. Ultrason., Ferroelectr., Freq. Control*, vol. 67, no. 5, pp. 943–956, May 2020.

[15] R. Ali, "Fourier-based synthetic-aperture imaging for arbitrary transmissions by cross-correlation of transmitted and received wavefields," *Ultrason. Imag.*, vol. 43, no. 5, pp. 282–294, Sep. 2021, doi: 10.1177/01617346211026350.

[16] F. Bureau, J. Robin, A. Le Ber, W. Lambert, M. Fink, and A. Aubry, "Three-dimensional ultrasound matrix imaging," *Nature Commun.*, vol. 14, no. 1, p. 6793, Oct. 2023. [Online]. Available: https://www.nature.com/articles/s41467-023-42338-8

[17] B. A. Angelsen, *Ultrasound Imaging: Waves, Signals, and Signal Processing: Basic Principles, Wave Generation, Propagation, and Beamforming in Homogeneous Tissue*, vol. 1. Trondheim, Norway: Emantec AS, 2000.

[18] J. P. Åsen and S. Holm, "Huygens on speed: Interactive simulation of ultrasound pressure fields," in *Proc. EEE Int. Ultrason. Symp.*, Oct. 2012, pp. 1643–1646. [Online]. Available: https://ieeexplore.ieee.org/document/6562157

[19] S. Holm, "Ultrasim—A toolbox for ultrasound field simulation," in *Proc. Nordic MATLAB Conf.*, Oslo, Norway, Oct. 2001, pp. 1–5.

[20] V. Perrot, M. Polichetti, F. Varray, and D. Garcia, "So you think you can DAS? A viewpoint on delay-and-sum beamforming," *Ultrasonics*, vol. 111, Mar. 2021, Art. no. 106309. [Online]. Available: https://www.sciencedirect.com/science/article/pii/S0041624X20302444

[21] T. L. Szabo, "Array beamforming," in *Diagnostic Ultrasound Imaging: Inside Out*, 2nd ed. Boston, MA, USA: Academic, Jan. 2014, ch. 7, pp. 209–255. [Online]. Available: https://www.sciencedirect.com/science/article/pii/B9780123964878000070

[22] M. D. Kvalevåg, "vbeam: A fast and differentiable beamformer for optimizing ultrasound imaging," in *Proc. IEEE Int. Ultrason. Symp. (IUS)*, Sep. 2023, pp. 1–4.

[23] J. Bradbury et al. (2018). *JAX: Composable Transformations of Python+NumPy Programs*. [Online]. Available: http://github.com/google/jax

[24] A. Rodriguez-Molares et al., "The ultrasound toolbox," in *Proc. IEEE Int. Ultrason. Symp. (IUS)*, Sep. 2017, pp. 1–4.

[25] N. Bottenus, "REFoCUS: Ultrasound focusing for the software beamforming age," in *Proc. IEEE Int. Ultrason. Symp. (IUS)*, Oct. 2018, pp. 1–4.

[26] A. Rodriguez-Molares et al., "The generalized contrast-to-noise ratio: A formal definition for lesion detectability," *IEEE Trans. Ultrason., Ferroelectr., Freq. Control*, vol. 67, no. 4, pp. 745–759, Apr. 2020.

OLE MARIUS HOEL RINDAL (Member, IEEE) was born in Hamar, Norway, in 1990. He received the M.S. degree in computer science (signal processing) from the University of Oslo (UiO), Norway, in 2014, and the Ph.D. degree with a dissertation entitled Software Beamforming in Medical Ultrasound Imaging-a Blessing and a Curse in 2019. He is currently a Senior Lecturer with UiO as well as the Co-Founder and a Technology Manager of the company Sonair AS.

His research interests include signal processing, beamforming, medical image formation, image processing, and machine learning, as well as physiological and biomechanical aspects of cross-country skiing.

ANDERS EMIL VRÅLSTAD (Graduate Student Member, IEEE) was born in Oslo, Norway, in 1997. He received the M.Sc. degree in electronic engineering and acoustics from the Norwegian University of Science and Technology (NTNU), where he is currently pursuing the Ph.D. degree with the Department of Circulation and Medical Imaging. His Ph.D. topic is on medical ultrasound beamforming, speed of sound, and machine learning.

His current research interests include ultrasound beamforming, aberration correction, and image quality enhancement.

MAGNUS DALEN KVALEVÅG (Member, IEEE) was born in Haugesund, Norway, in 1995. He received the M.Sc. degree in informatics (programming and system architecture) from the University of Oslo (UiO). He is currently pursuing the Ph.D. degree with the Department of Circulation and Medical Imaging, NTNU. His Ph.D. topic is on combining software beamforming for medical ultrasound with machine learning.

His current research interests include ultrasound beamforming and GPU processing.

SVEIN-ERIK MÅSØY was born in Halden, Norway, in 1975. He received the M.Sc. degree in applied mechanics, thermodynamics, and fluid dynamics and the Ph.D. degree from the Norwegian University of Science and Technology (NTNU), Trondheim, Norway, in 1999 and 2004, respectively. His Ph.D. dissertation entitled Estimation and Correction of Aberration in Medical Ultrasound Imaging.

He is currently an Associate Professor with the Department of Circulation and Medical Imaging, NTNU. His current research interests include beamforming, machine learning, and non-destructive testing using ultrasound.